



**HAL**  
open science

# The Mechanisms Leading to a Stratospheric Hydration by Overshooting Convection

Thibaut Dauhut, Jean-Pierre Chaboureau, Peter H Haynes, Todd P Lane

► **To cite this version:**

Thibaut Dauhut, Jean-Pierre Chaboureau, Peter H Haynes, Todd P Lane. The Mechanisms Leading to a Stratospheric Hydration by Overshooting Convection. *Journal of the Atmospheric Sciences*, 2018, 75 (12), pp.4383-4398. 10.1175/JAS-D-18-0176.1 . hal-04253976

**HAL Id: hal-04253976**

**<https://hal.science/hal-04253976>**

Submitted on 23 Oct 2023

**HAL** is a multi-disciplinary open access archive for the deposit and dissemination of scientific research documents, whether they are published or not. The documents may come from teaching and research institutions in France or abroad, or from public or private research centers.

L'archive ouverte pluridisciplinaire **HAL**, est destinée au dépôt et à la diffusion de documents scientifiques de niveau recherche, publiés ou non, émanant des établissements d'enseignement et de recherche français ou étrangers, des laboratoires publics ou privés.

Copyright

# The Mechanisms Leading to a Stratospheric Hydration by Overshooting Convection

THIBAUT DAUHUT AND JEAN-PIERRE CHABOUREAU

*Laboratoire d'Aérodynamique, Université de Toulouse, CNRS, UPS, Toulouse, France*

PETER H. HAYNES

*Department of Applied Mathematics and Theoretical Physics, University of Cambridge, Cambridge, United Kingdom*

TODD P. LANE

*School of Earth Sciences, and Australian Research Council Centre of Excellence for Climate Extremes,  
University of Melbourne, Melbourne, Victoria, Australia*

(Manuscript received 22 June 2018, in final form 4 October 2018)

## ABSTRACT

Overshoots are convective air parcels that rise beyond their level of neutral buoyancy. A giga-large-eddy simulation (100-m cubic resolution) of “Hector the Convective,” a deep convective system that regularly forms in northern Australia, is analyzed to identify overshoots and quantify the effect of hydration of the stratosphere. In the simulation, 1507 individual overshoots were identified, and 46 of them were tracked over more than 10 min. Hydration of the stratosphere occurs through a sequence of mechanisms: overshoot penetration into the stratosphere, followed by entrainment of stratospheric air and then by efficient turbulent mixing between the air in the overshoot and the entrained warmer air, leaving the subsequent mixed air at about the maximum overshooting altitude. The time scale of these mechanisms is about 1 min. Two categories of overshoots are distinguished: those that significantly hydrate the stratosphere and those that have little direct hydration effect. The former reach higher altitudes and hence entrain and mix with air that has higher potential temperatures. The resulting mixed air has higher temperatures and higher saturation mixing ratios. Therefore, a greater amount of the hydrometeors carried by the original overshoot sublimates to form a persistent vapor-enriched layer. This makes the maximum overshooting altitude the key prognostic for the parameterization of deep convection to represent the correct overshoot transport. One common convection parameterization is tested, and the results suggest that the overshoot downward acceleration due to negative buoyancy is too large relative to that predicted by the numerical simulations and needs to be reduced.

## 1. Introduction

Overshooting convection corresponds to deep convective systems in which convective turrets penetrate higher than the level of neutral buoyancy. It has been estimated (Liu and Zipser 2005) that in the tropics, 0.1% of convective systems produce overshoots that penetrate higher than the cold-point tropopause, located around 17-km altitude (Munchak and Pan 2014). As tropospheric air enters the stratosphere primarily in the tropics, global stratospheric composition is largely determined by tropical cross-tropopause transport (Fueglistaler et al. 2009; Randel and Jensen 2013).

There has been a long-running debate on the contribution of deep convection to tropical cross-tropopause transport. The convective contribution is currently often considered rather small compared to the total transport mainly attributed to the large-scale slow ascent. However, recent research continues to highlight the potential role of deep convection in affecting stratospheric composition (Pommereau 2010; Anderson et al. 2012; Virts and Houze 2015; Dauhut et al. 2015; Smith et al. 2017). Observational and modeling studies show in particular the moistening effect of overshooting convection on the stratosphere (Chaboureau et al. 2007; Grosvenor et al. 2007; Jensen et al. 2007; Corti et al. 2008; Khaykin et al. 2009; de Reus et al. 2009; Chemel et al. 2009; Avery et al. 2017). Isotopologue studies and climate projections further emphasize the role of the lofting of ice

---

*Corresponding author:* Thibaut Dauhut, thibaut.dauhut@aero.obs-mip.fr

particles by convection in affecting the stratospheric humidity (e.g., Sayres et al. 2010; Steinwagner et al. 2010; Dessler et al. 2016). There are currently strong biases in temperature and humidity around the tropopause in climate models, which have too-coarse resolution to explicitly reproduce convective injection (e.g., Hardiman et al. 2015), and improving the model representation of this process is one candidate for reducing the current biases.

The morphology of convective systems that reach the stratosphere and of the overshoots at their top is understood in broad terms. The convective systems that lead to tropopause penetration by the overshoots are primarily large, organized mesoscale systems (Rossow and Pearl 2007; Virts and Houze 2015). The overshoots exhibit a variety of shapes. Wang (2003) reported from his numerical simulation in the midlatitudes two different types of overshooting tops: anvil sheet plumes and overshooting plumes. Fujita (1989) described five types of above-anvil clouds (clean overshooting dome, curly-hair cirrus, fountain cirrus, flair cirrus, and geyser cirrus), most being directly linked to overshooting convection, and further illustrated them with photographs of clouds around the tropopause in the midlatitudes. As reported by Homeyer et al. (2017) from satellite and ground-based radar measurements in midlatitudes, the overshoots can evolve into above-anvil cirrus plumes with significant horizontal extension. Still, satellite instruments may not have enough temporal and spatial resolution to capture the fast-evolving, small overshoots, underestimating the maximum overshooting altitude for instance (Sherwood et al. 2004). One of the objectives of this study is to provide for the first time, exploiting a specially designed high-resolution numerical simulation, a detailed characterization of the morphology and properties of overshoots in the tropics.

The processes inside the overshoots that determine their impact on the stratospheric composition are particularly difficult to observe, and our understanding relies on limited in situ measurements and numerical modeling. The overshoots promote strong mixing between tropospheric and stratospheric air, with effective transport of constituents both upward and downward (Frey et al. 2015). The strong vertical wind velocities generate gravity waves (Lane 2008) that break and promote the transport across isentropic surfaces (Wang 2003). At smaller scales, some mixing is induced by the growth of unstable modes of cloud boundary instabilities (Grabowski and Clark 1991, 1993a). The quantitative roles of the wave breaking and the cloud boundary instabilities in generating mixing remain unclear. The impact of the overshoots on the water vapor content depends furthermore on the background relative humidity, and when there is subsaturation, some

hydration is expected (Jensen et al. 2007; Hassim and Lane 2010). Numerical and observational studies mention that a substantial fraction of the ice hydrometeors in the overshoots are small enough not to sediment directly back to the troposphere after injection in the stratosphere but rather have sufficient residence time to sublimate and lead to hydration (Jensen et al. 2007; Corti et al. 2008; de Reus et al. 2009). Radiometer measurements from the Microwave Limb Sounder further indicate that convectively lofted ice can contribute significantly to the total water content near the tropical cold point (Wu et al. 2005).

This study aims to provide quantitative details to describe the overshoots that reach the stratosphere. The scientific questions are as follows: How many overshoots can one very deep convective system produce? How much water is transported by each overshoot? How local and transient are the overshoots? And what are the key processes that determine whether an overshoot hydrates the stratosphere? The investigations provide unprecedented characterization of the population of the overshoots above a very deep convective system and describe their variety of characteristics and effects on the local stratosphere.

The very deep convective system on which the study focuses is an Australian tropical multicellular storm commonly called “Hector the Convectur.” The case of 30 November 2005 is selected, when some overshoots were observed beyond 18-km altitude (Corti et al. 2008). A large-eddy simulation (LES) of this event is used to describe the population of overshoots on the top of Hector and to investigate the small-scale processes that lead to the hydration of the stratosphere with about  $3 \times 10^6$  kg of water (Dauhut et al. 2015). The simulation, called giga-LES (cubic grid of 100 m and more than 1 billion grid points) was run with the Meso-NH model (Lafore et al. 1998; Lac et al. 2018). It has sufficient resolution to describe the detailed characteristics of the overshoots. The 100-m vertical and horizontal grid spacing is important to reproduce the correct cloud-top altitude (Homeyer 2015), to capture a significant part of the inertial range in the energy cascade by the cloud eddies (Dauhut et al. 2016), and to give a robust estimate of the hydration by the overshoots (Dauhut et al. 2015, 2017). During the period of development of the overshoots into the stratosphere (the very deep convective phase), the model has been rerun to obtain high-frequency outputs—one every minute.

Few previous studies investigated the processes related to the overshoot transport from numerical simulations of very deep convective systems. Wang (2003) analyzed the transport of water across the tropopause by a case of overshooting convection in midlatitudes.

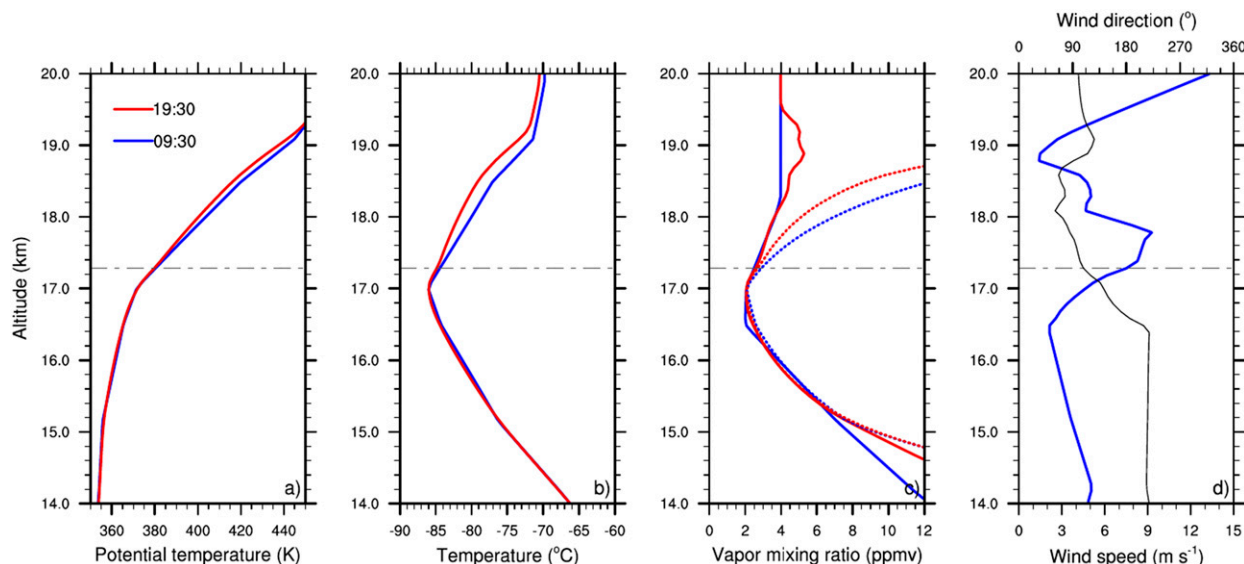


FIG. 1. Vertical profiles at the beginning (blue) and at the end (red) of the simulation of the environmental (a) potential temperature, (b) temperature, and (c) water vapor mixing ratio (solid lines) and saturation water vapor mixing ratio (dotted lines). (d) Vertical profiles at the beginning of the simulation of the environmental wind velocity (blue) and wind origin (black; 90° means from east). The dashed gray line is the tropopause at 380-K potential temperature.

Based on a simulation with 1-km resolution, he focused on two overshoots to highlight two different modes of transport and the underlying processes. Gravity wave breaking appeared crucial. Our study contrasts from his as we use 10-times-finer horizontal resolution and as we investigate the whole population of overshoots above the very deep convective system. Lane and Sharman (2006) investigated also the mixing above a very deep convective system, with a 150-m-resolution simulation, but they focused on the gravity wave generation and breaking, especially above the cloud. In our study, we will show that the mixing inside the overshoots is of primary importance.

The model and the method used to identify and track the overshoots are described in section 2. The hydration of the stratosphere by the overshoots is investigated in section 3, where the key mechanisms for the hydration are highlighted. The capability of the Meso-NH model to represent the overshoot transport, when the model cannot resolve explicitly the convection, which must instead be represented by parameterization, is analyzed in section 4. A discussion of our results is proposed in section 5, and the conclusions are given in section 6.

## 2. Model design and tracking method

### a. Meso-NH large-eddy simulation

The simulation (Dauhut et al. 2015, 2016) is run with the anelastic nonhydrostatic mesoscale model Meso-NH

(Lafore et al. 1998; Lac et al. 2018). The domain of  $256 \text{ km} \times 204.8 \text{ km}$  is centered over the Tiwi Islands, 100 km north of Darwin, Australia. The domain is large enough to ensure that the domain edges, where open boundary conditions apply, do not affect the development of the Hector system. The model has 256 levels that follow the smooth orography (hills not higher than 80 m). The model top is at 25-km altitude, with a sponge layer in the uppermost 3 km to prevent the reflection of gravity waves. The vertical and horizontal grid spacing is 100 m, to resolve the overshoots and the mixing of tropospheric and stratospheric air by the large overshoot eddies, except that the vertical spacing is reduced (down to 40 m) close to the surface. Parameterizations are used to represent the microphysics (a single-moment scheme with three ice hydrometeor species: cloud ice, snow, and graupel), turbulence (3D scheme based on 1.5-order closure), radiation, and surface exchanges [further details in Dauhut et al. (2016)]. The sea surface temperature is fixed at 29°C. The soil temperature and moisture are initialized at 30°C and  $0.16 \text{ m}^3 \text{ m}^{-3}$ , respectively, and evolve with time. No large-scale dynamical forcing is applied.

Over the whole domain, the atmosphere is homogeneously initialized in temperature, humidity, horizontal wind intensity, and direction with the sounding taken in Darwin on 0000 UTC (0930 LT) 30 November 2005 (Fig. 1). Between 13- and 17-km altitudes, the water vapor profile is extended with the water vapor content

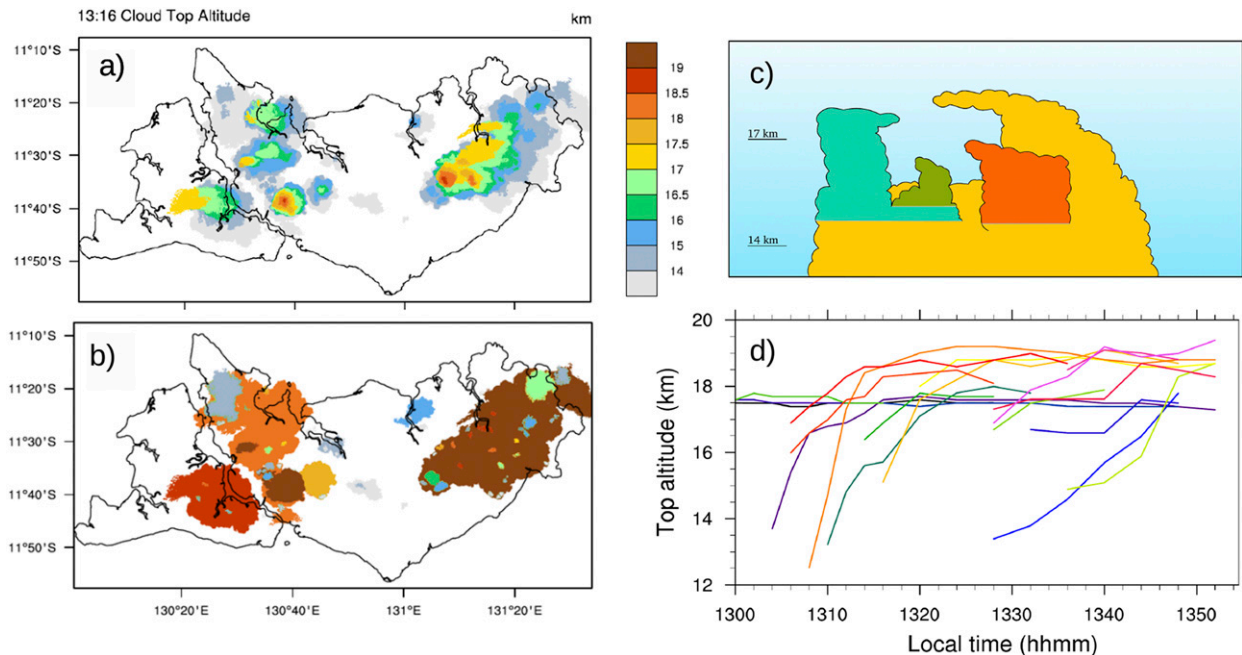


FIG. 2. (a) Map of the cloud-top altitude at 1316 LT. (b) Map at the same time of the overshoots defined as connected regions where ice water content is beyond  $10^{-5} \text{ kg kg}^{-1}$  (16 eq. ppmv); each individual overshoot is shaded with a unique bright color. (c) Schematic of the overshoot identification, lateral view of four individual overshoots, shaded with different bright colors. (d) Time evolution of the top altitude for all the overshoots that reach the stratosphere, listed in Tables 1 and 2. In (d), the nonhydrating overshoots are in black and blue, and the hydrating overshoots are in green, yellow, orange, red, and pink, from the least hydrating to the most.

from the ECMWF analysis. Above 17 km, the water vapor content is set following the observations reported by Corti et al. (2008), from 2 ppmv at 17 km (380-K potential temperature) to 4 ppmv at 18 km (410 K) and homogeneously equal to 4 ppmv aloft. The initial temperature, humidity, and wind profiles are maintained at the boundary and are intended to correspond to the oceanic environment. For analysis purposes, the tropopause is defined as the 380-K isentropic surface (at 17.3 km) that matches the cold point in the undisturbed environment. In the tropical tropopause layer (TTL; between 14- and 20-km altitudes), the overshoots grow through subsaturated and saturated layers (Fig. 1c). The simulation lasts 10 h, and the overshoots reach the stratosphere for the first time after 3.5 h of convective development, that is, around 1300 LT. Air parcels that ultimately reach equilibrium at potential temperatures higher than 380 K are considered irreversibly transported into the stratosphere.

### b. Overshoot identification and tracking

The overshoots are defined as individual connected three-dimensional regions where the hydrometeor content exceeds a threshold of  $10^{-5} \text{ kg kg}^{-1}$  (equivalent to 16 ppmv in the vapor phase; Figs. 2a–c). Little sensitivity to the threshold of the hydrometeor content is expected

since strong gradients are observed at the interface between the overshoots and the environmental air. Visual inspection confirms the validity of the chosen threshold value. A clustering algorithm allows us to distinguish the different overshoots by giving an identity number to each. The overshoots are identified in each 3D field (snapshot) that corresponds to one time, with identification starting from the top of the model and going down to 12 km (to characterize the overshoots down to a few kilometers below the TTL). If at some level, a cloud region can be associated with several overshoots, it is identified as part of the widest overshoot (Fig. 2c). One single overshoot may have different identity numbers at different times.

The tracking of the overshoots consists in following the individual overshoots and the changes along time of their identity number. The list of the successive identity numbers of one single overshoot is one track. The method is the following: each 3D field of the identity numbers is reduced to a 2D projection that corresponds to what one would see from above (Fig. 2b). The successive 2D projections are then compared. Two identity numbers at two successive times are part of one track if the two projections overlay. When several overshoot projections overlay one at the previous time, the 3D distance between the overshoot tops are compared.

The overshoot whose top is the closest to the top of the overshoot at the previous time is selected. If none of the overshoots overlays one at the previous time, the corresponding track ends. Such a tracking method allows us to compute the evolution of the characteristics of the overshoots along their life cycle, like the altitude of their top (Fig. 2d). Among the overshoots that reach the stratosphere, three already have their top around 17 km at 1300 LT. The others exhibit a fast ascent (up to  $1 \text{ km min}^{-1}$ ), they reach a maximum overshooting altitude (climax time), and then their top stays at an almost constant altitude close to the maximum overshooting altitude.

No threshold on the size of the identified overshoots is used. This leads to nearly flat local tops in undulated cloud interfaces being considered as overshoots as well as prominent cloud tops. However, the flat local tops are, in practice, transient and quickly lost by the tracking algorithm. To filter them out, a threshold is used on the tracking duration. In total, 1507 tracks are produced, among which 46 only last more than 10 min. For the remainder of this paper, the focus is on these 46 long-lasting overshoots.

### 3. Stratosphere hydration by the overshoots

As may be seen from Fig. 3, the development of Hector up to the stratosphere is gradual. The cumulonimbus that compose Hector from 1215 LT onward reach the stratosphere for the first time shortly before 1300 LT (Fig. 3a). At that time, strong localized convergence of humidity is produced at the surface by the cold pool dynamics, and very intense updrafts develop and experience weak dilution (Dauhut et al. 2016). The ice hydrometeors are injected into the stratosphere by the overshoots during 1 h only, from 1300 to 1400 LT. Then a part precipitates back to the troposphere, and the other part sublimates, leading to a net stratospheric hydration of  $2.776 \times 10^6 \text{ kg}$  in the form of two large vapor-enriched air pockets (Dauhut et al. 2015). The lowest TTL is hydrated by the first overshoots that reach it from about 1215 LT (Fig. 3b). The stratosphere is significantly hydrated (up to more than 1 ppmv in average over the domain) after 1345 LT. The decrease in the stratospheric humidity anomaly after 1830 LT is due to the advection of the vapor-enriched air pockets out of the domain by the intense stratospheric winds (Fig. 1d).

Still at the large scale, whereas the tropospheric part of the TTL (between 14- and 17.3-km altitudes) is warmed by the cloud development (up to about  $0.6^\circ\text{C}$ ), the lower stratosphere is cooled down by a few degrees (Fig. 3c). The stratosphere cooling starts 2 h before the first overshoots reach the stratosphere. At that time, the

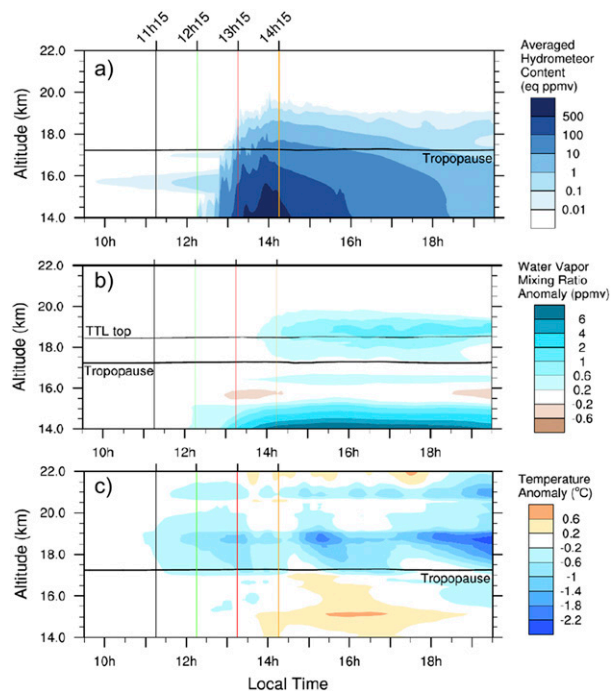


FIG. 3. Averages over the Tiwi Islands of (a) the hydrometeor mixing ratio, (b) the water vapor anomaly, and (c) the temperature anomaly. Anomalies are computed with reference to the initial profile. The tropopause and the TTL top are defined as the isentropic surfaces at 380- and 420-K potential temperature, respectively.

clouds extend to 5 km only. An explanation of this cooling is the adjustment to hydrostatic via gravity waves (Holloway and Neelin 2007; Kim et al. 2018). The convection generates a pressure gradient well above itself, producing divergent wind and broad ascent. The adiabatic ascent leads to a cooling, particularly visible near and above the tropopause, where the potential temperature lapse rate is larger than in the free troposphere. Given the local lapse rate, the net stratosphere cooling down to  $-2 \text{ K}$  corresponds to a general upward displacement of about 100 m. This hydrostatic adjustment occurs on a short time scale with respect to convection. The cooling persists during the whole cloud development, with fluctuating intensity, and increases at the end of the simulation. The large-scale upper-level cooling effect of the convection is consistent in terms of amplitude and altitude with what has been observed, for example, the GPS radio occultation measurements reported by Kim et al. (2018). Their measurements further indicate that such stratospheric cooling can occur over a large horizontal scale (about 6000 km) and can last several weeks. The present study is not focused on the stratosphere cooling. It highlights that, despite the temperature decrease, the humidity does increase

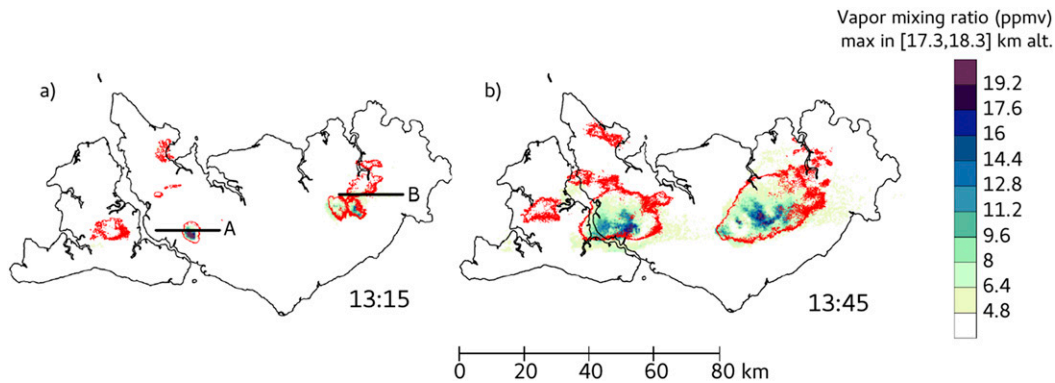


FIG. 4. Maps of the water vapor mixing ratio, maximum between 17.3- and 18.3-km altitude (blue) overlaid with the overshoot contours at the tropopause (mixing ratio of  $10^{-5} \text{ kg kg}^{-1}$ , i.e., 16 eq. ppmv, at 17-km altitude; red contours), at (a) 1315 and (b) 1345 LT. In (a), the solid lines labeled A and B are the locations of the vertical sections across the hydrating overshoot A and the nonhydrating overshoot B (Figs. 5a,b), respectively.

because of ice sublimation and the large preexisting subsaturation of the background lower stratosphere.

#### a. Hydrating and nonhydrating overshoots

The horizontal sections at 17 km shown in Fig. 4 of the overshoots that reach the stratosphere highlight how diverse the overshoots are in terms of size and shape. All these overshoots inject ice hydrometeors into the stratosphere, but some only produce vapor-enriched air pockets at their top, leading to local vapor mixing ratios between 4 (the background value) and 20 ppmv. At 1315 LT, less than 10 overshoots have crossed the tropopause. The effective width of each at 17 km is less than 15 km, and most of them are well separated. At 1345 LT, some of the overshooting clouds have merged at the tropopause level. The two largest overshooting areas are located in the middle of the Tiwi Islands, where the convergence lines at the surface developed at their strongest intensity (Dauhut et al. 2016).

Among all tracked overshoots that reach the stratosphere, two subpopulations of overshoots can be distinguished: the hydrating overshoots, which lead to subsequent hydration of the stratosphere (Table 1), and the nonhydrating overshoots, leading to insignificant hydration of the stratosphere or low dehydration (Table 2). It is important to note that (i) hydration and dehydration are defined here in terms of impacts on the water vapor field, not the total water field, and (ii) the terms “hydrating” and “nonhydrating” are being used as a shorthand and nonhydrating does not mean exactly zero hydration effect. The nonhydrating overshoots reach in general lower top altitudes than the hydrating overshoots. The amplitude of the hydration is driven by both the top altitude and the apparent width of the overshoot. In the following subsections, two overshoots, the hydrating overshoot A and the nonhydrating overshoot B, are chosen to be analyzed in order to highlight the mechanisms that determine the capability of the

TABLE 1. Description of the overshoots that reach the stratosphere. Overshoot climax is when it reaches its maximum overshooting altitude. First subpopulation: the hydrating overshoots.

Overshoot	Maximum overshooting altitude (km)	Climax time (LT)	Climax effective width (km)	Stratosphere hydration ( $\times 1000 \text{ kg}$ )
E	19.386	1352	79.657	67.617
F	19.096	1340	64.258	49.061
C	18.985	1332	53.398	29.323
G	18.688	1344	48.066	34.823
H	18.485	1324	44.493	7.068
D	17.786	1302	24.099	0.189
A	19.199	1328	4.759	3.626
J	19.093	1340	3.649	1.529
K	18.887	1336	4.889	1.121
L	18.686	1352	1.221	0.258
O	17.886	1340	2.798	0.205
N	17.785	1320	3.400	0.102

TABLE 2. As in Table 1, but for the second subpopulation: the nonhydrating overshoots.

Overshoot	Maximum overshooting altitude (km)	Climax time (LT)	Climax effective width (km)	Stratosphere hydration ( $\times 1000$ kg)
M	17.990	1328	2.722	0.013
I	17.686	1320	12.713	-0.254
B	17.592	1302	18.257	-0.191
Q	17.786	1348	1.215	-0.013
R	17.590	1344	1.854	-0.021
P	17.589	1320	10.034	-0.359
S	17.491	1324	1.359	0.002

overshoots to hydrate the stratosphere and also to contrast the characteristics of the two subpopulations. Their locations at the top of the cloud system are illustrated in Figs. 5a and 5b, respectively, at times when they have already reached the tropopause and the underlying updrafts are still active.

### b. Mechanisms leading to hydration

Overshoot A, which leads to hydration, is first investigated. It is located at the top of one intense updraft (Fig. 5a). The overshoot evolution is analyzed with successive vertical cross sections, one every minute (Fig. 6, left). As the overshoot grows, the isentropic surfaces are compressed together. At 1314 LT, the cold and dry air mass that constitutes the overshoot collapses, entraining some stratospheric air into the top of the cloud as it descends, as shown by the steep slope of the isentropic surfaces. At the overshoot top altitude (18.5 km), where the stratospheric air comes from, the environmental air is subsaturated with less than 30% relative humidity

(Fig. 1). A vapor-enriched region appears where the stratospheric air mixes with the cloud. It can be explained by the sublimation of some ice hydrometeors as they mix with the warmer, subsaturated stratospheric air. The disturbed shapes of the isentropic surfaces between 1314 and 1316 LT highlight the strong mixing produced in the overshoot. This strong mixing is mostly due to the large wind shear at the interface between the dry inner core of the overshoot (where divergent winds show horizontal velocities larger than  $20 \text{ m s}^{-1}$ ) and the hydrated region aloft, made of a mixture of tropospheric and stratospheric air. Some gravity wave activity is suggested by the rise and descent of the isentropic surfaces over time. The breaking of gravity waves may contribute to the intense mixing. The very strong vertical gradient of potential temperature (visible by the superposition of many isentropic surfaces) relaxes back to environmental value about 10 min later (not shown). However, the undulations of the isentropic surfaces persist, and the humid air pocket stays at the top of the cloud (then at about 19.5-km altitude).

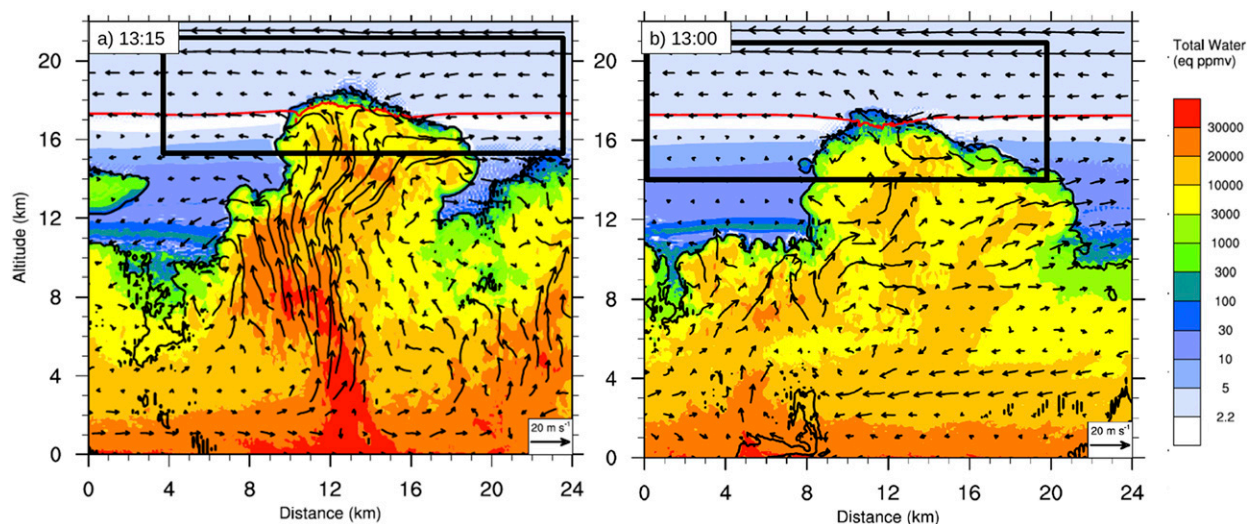


FIG. 5. Vertical cross sections of the total water content showing the updrafts below (a) the hydrating overshoot A and (b) the nonhydrating overshoot B. The rectangles in (a) and (b) show the locations of the cross sections in Fig. 6 (left) and Fig. 6 (right), respectively. The red line is the tropopause at 380-K potential temperature.



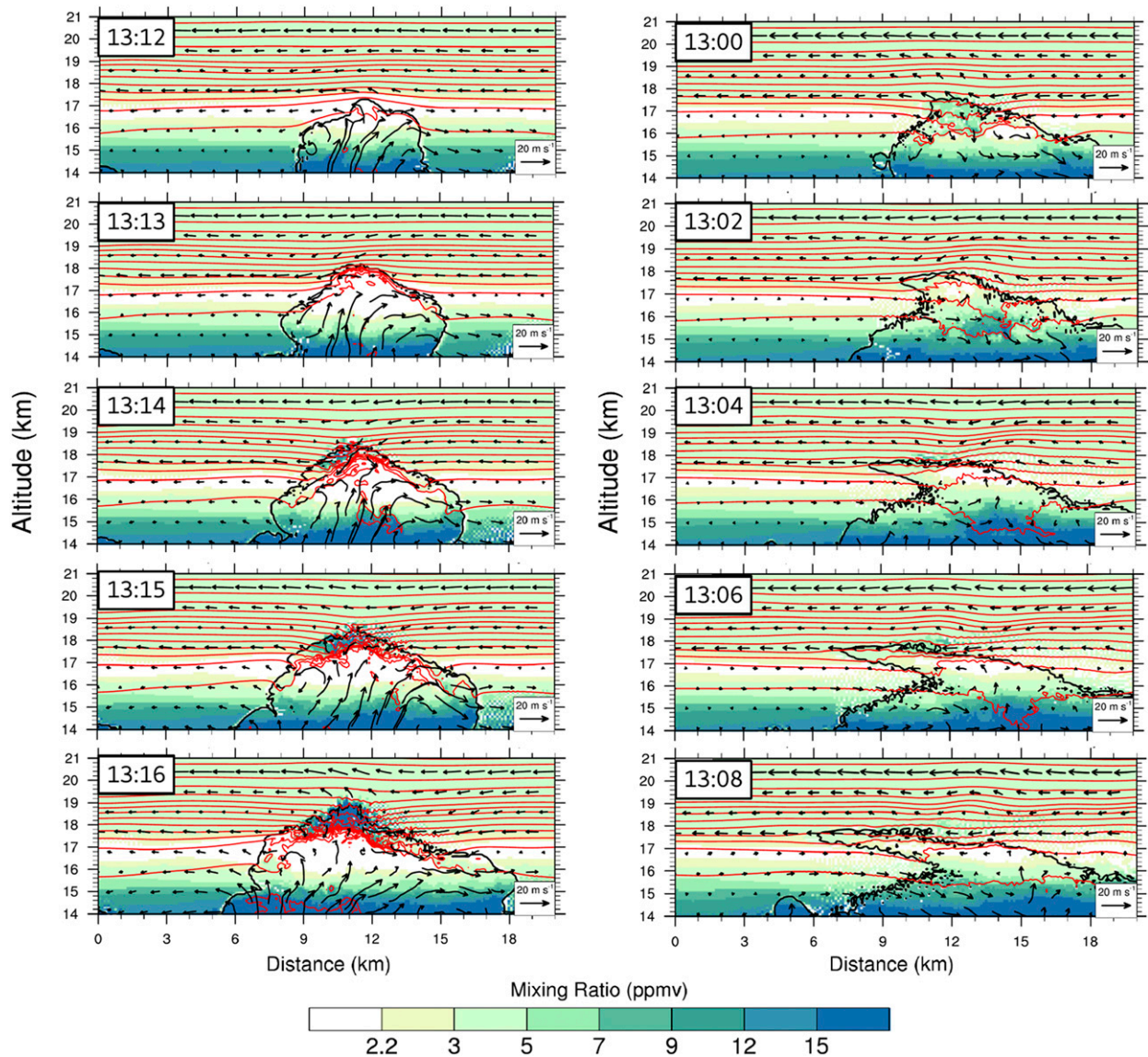


FIG. 6. Vertical cross sections of the water vapor mixing ratio (left) every 1 min across the hydrating overshoot A and (right) every 2 min across the nonhydrating overshoot B. The locations of the cross sections are shown in Fig. 5. The red lines are the isentropic surfaces every 10 K; the lowest one outside the overshoots (at about 15.8-km altitude) is at 360-K potential temperature.

The potential temperature inside the humid pocket at that time displays typical values of the lower stratosphere (larger than 380 K). This shows the cross-isentropic transport of water and suggests the importance of the entrainment at the top of the overshoot of stratospheric air for the injected water vapor to stay in the stratosphere.

Overshoot B, which produces no hydration, is now analyzed. The updraft above which it develops is weaker (Fig. 5b). At 1300 LT, when the first high-frequency output is available (Fig. 6, right), some stratospheric air is already entrained and mixed inside the overshoot top, where the humidity is slightly larger than in the

environment at the same level. However, as the overshoot top continues to grow, the humidity inside decreases back to environmental values. The overshoot is then stretched by the shear of the lower-stratosphere winds, leading to a cloudy layer. Small instabilities appear at the top of the cloudy layer, made visible by the disturbed cloud contour, but without any hydration. The isentropic surfaces undulate, but the mixing is not as strong as in the case of the overshoot A.

Overshoots A and B have similar sizes but contrast in shape, with overshoot B producing an elongated, horizontal cloudy layer. In that sense, overshoot A corresponds

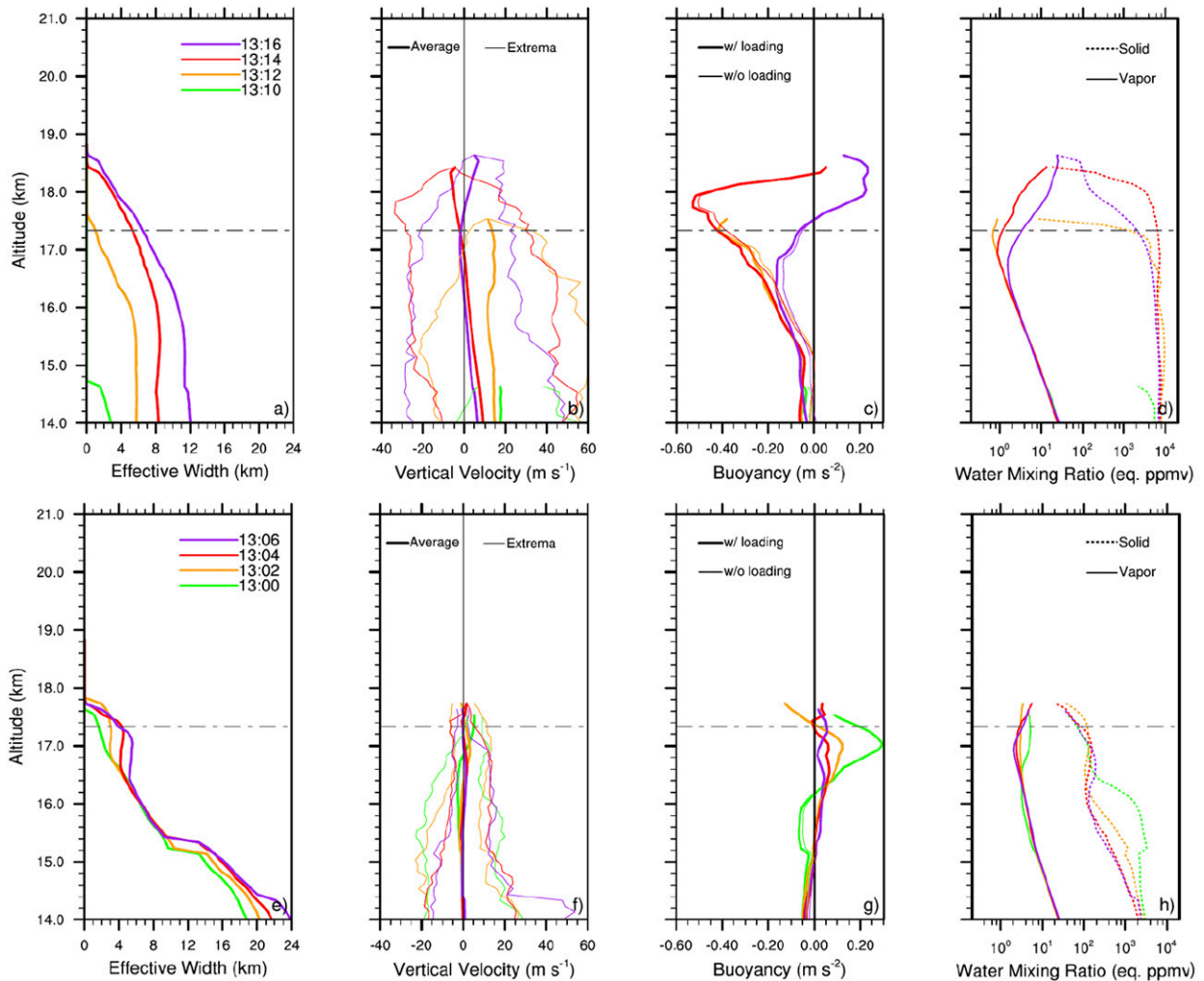


FIG. 7. Vertical profiles of the (a),(e) effective width, (b),(f) average and extreme vertical velocities, (c),(g) average buoyancy, and (d),(h) water mixing ratio for the (a)–(d) hydrating overshoot A and (e)–(h) nonhydrating overshoot B. The dotted–dashed gray line is the tropopause at 380-K potential temperature. In (c) and (g), the thick and thin lines are the buoyancy profiles taking and not taking into account the hydrometeor loading, respectively.

to the clean overshooting-dome category of the anvil-top clouds by Fujita (1989) and overshoot B to the curly-hair cirrus category by Fujita (1989) or to the overshooting plume category of Wang (2003) characterized by a chimney plume shape. From Fig. 6, it is also visible that the overshoot A presents larger vertical velocities than overshoot B and that the water is transported as ice inside the dry inner core of the overshoot [similar to that in Figs. 3 and 6 of Wang (2003)].

The characteristics of the two overshoots are further investigated with vertical profiles of their effective width, vertical velocities, buoyancy, and water mixing ratio (Fig. 7). The effective width is defined as the diameter of a circle that has the same area as the overshoot section. The profiles are given for each updraft every

2 min, around the time when they reach the stratosphere. From the vertical profiles, it is clear that overshoot A reaches higher altitudes than overshoot B. Both overshoots exhibit enlargement with time (Figs. 7a,e). In contrast with overshoot A, overshoot B exhibits a secondary maximum of the effective width, which corresponds to the cloudy layer at the tropopause. Overshoot B is also twice as large as overshoot A at the base of the TTL (14 km), but its top is about 1 km lower than the top of overshoot A. The effective widths of both overshoots are in excellent agreement with the mean cloud area in the TTL for composites of overshooting convection, as reported by the observational study of Hassim et al. (2014) (and corrected for observational biases). The vertical velocities inside overshoot A exhibit larger

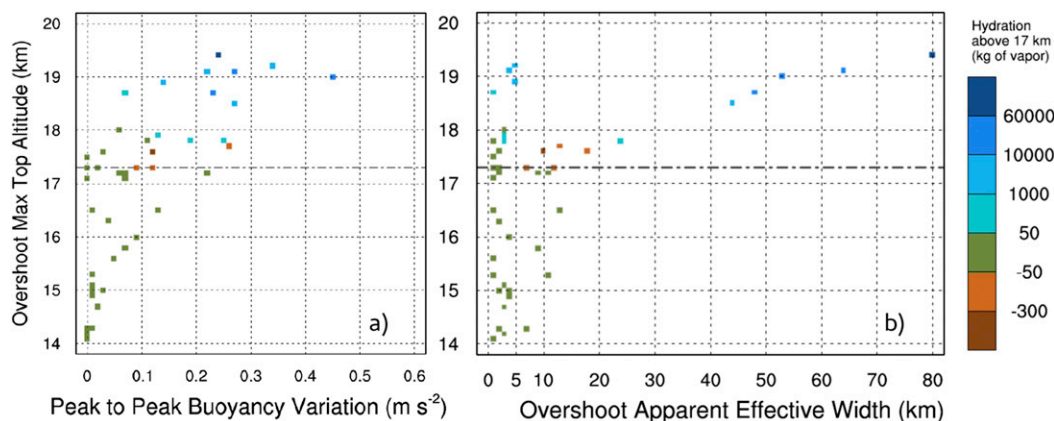


FIG. 8. Distribution of the overshoots as function of their maximum top altitude and (a) the peak-to-peak amplitude of their buoyancy variations and (b) their apparent effective width at the time of the maximum top altitude. Each square represents one overshoot; its color scales with the hydration led by the overshoot. The dotted–dashed gray line is the tropopause at 380-K potential temperature.

average and extreme values than overshoot B, about  $15 \text{ m s}^{-1}$  on average and  $20\text{--}60 \text{ m s}^{-1}$  as maximum at 1312 LT (Figs. 7b,f). Afterward, the average vertical velocities at the top of overshoot A are oscillating in time around zero, indicating the presence of gravity waves. At the same time, very large values of buoyancy are found also at the top of overshoot A (Fig. 7c), first negative, not because of the hydrometeor loading but because of its low temperature (as it can be deduced from the comparison between the profile that takes into account the hydrometeor loading and the one that does not), and then positive. The very large increase in buoyancy with altitude at 1314 LT is a signature of the entrainment of warmer stratospheric air at the top of overshoot A. The buoyancy profile of overshoot A at 1316 LT suggests that the large absolute values oscillate about zero with time, likely because of the presence of gravity waves. The positive buoyancy peak at the top of overshoot B at 1300 LT also suggests the entrainment of warmer air from the top but without any evidence for later gravity wave oscillations. The lower static stability below the 380-K tropopause than above may explain why fewer gravity waves are excited by overshoot B than by A. Overshoot A shows also large values of ice mixing ratio (Fig. 7d), about  $7000 \text{ eq. ppmv}$  ( $4 \text{ g kg}^{-1}$ ), constant in time and uniform along the altitude, until 1316 LT when a significant amount of ice sublimates and the vapor mixing ratio increases between 16.5- and 18.5-km altitudes. In contrast, overshoot B carries less ice in the TTL. The slight increase of water vapor at 1300 LT by overshoot B is compensated by condensation a few minutes later.

At later time (not shown), the cloudy layer produced by overshoot B is continuously stretched by

the stratospheric winds. Some ice at its very top sublimates, leading to small, very localized hydration around 18-km altitude. The track of overshoot B is then lost as other overshoots develop in its vicinity. Similar inspection of the other nonhydrating overshoots indicate that this process is not systematic: the cloudy layer of overshoots P and I for instance continue to stretch in a low-temperature anomaly, producing no stratosphere hydration on a short time scale. Their track is lost as the dilution decreases the ice content below the threshold for overshoot detection.

The entrainment of stratospheric air at the top of the overshoot, which is found to be crucial for a significative hydration of the stratosphere, corresponds to the secondary circulation described by Lane (2008), who showed that penetrative convection generates a succession of vortices with alternate directions. Half of them induce environmental air to flow downward across the overshoot top. This entrainment of stratospheric air may also be explained by the obstacle effect, as discussed in Lane et al. (2001): the cloud partially blocks the horizontal wind and produces a downward flow across its top.

### c. Key parameters for hydration

The mechanism that appears key for the hydration of the stratosphere is the entrainment of stratospheric air into the top of the overshoots. This “top entrainment” of stratospheric air has a marked signature in the vertical profiles of the hydrating overshoot A: the average buoyancy exhibits large variations. To check whether this mechanism is at play for all the overshoots that hydrate the stratosphere, we compute the difference between the maximum and the minimum in the average

buoyancy vertical profile for each overshoot that lasts more than 10 min, at the time of their maximum overshooting altitude (Fig. 8a). The hydration is computed as the integral of the water vapor anomaly (relative to the initial profile) inside each overshoot. All the overshoots that show the largest buoyancy variations (more than  $0.27 \text{ m s}^{-2}$ ) are indeed hydrating the stratosphere. These large buoyancy variations are explained by the top entrainment mechanism and by the large potential temperature of the background stratospheric air that is entrained at high altitude.

Consistent with that description, the amplitude of the stratosphere hydration is the largest for the overshoots that reach the highest altitudes. The two subpopulations of the hydrating overshoots (blue in Fig. 8) and the nonhydrating overshoots (green and brown) are separated by a threshold altitude at 17.8 km. This threshold altitude is slightly above the 380-K tropopause, above which the stratospheric air is subsaturated (Fig. 1). Interestingly, we found that a small subset of the nonhydrating overshoots (four) are actually dehydrating the stratosphere. The top of these overshoots is located in the lowermost stratosphere, between 17.3- and 17.8-km altitudes. In this region, these overshoots develop in a low-temperature anomaly, which results in water vapor contents lower than in the initial profile. The computation of the overshoot base effective width at the time of their maximum altitude (Fig. 8b) indicates that the most hydrating overshoots are also the ones with the largest bases, up to 80-km width, but about half of the hydrating overshoots also present a small base effective width of a few kilometers. Note however that our computation of the overshoots base width is limited as the identification algorithm leads to overshoots with very different depths (Fig. 2c), and one overshoot that is identified down to the TTL base has likely a larger base than an overshoot identified across a shallow layer.

The presence of top entrainment of stratospheric air is confirmed at the scale of the hydrating overshoot population. The maximum overshooting altitude appears to be a sufficient parameter to determine whether the overshoots will or will not hydrate the stratosphere for this case. For this reason, it is important for any model used to investigate the impact of convective transport into the stratosphere to capture the maximum overshooting altitude well. Beside the environmental thermal structure, this parameter is determined by the vertical velocity of the overshooting air parcels (Adler and Mack 1986), and their effective width, as wider air parcels are expected to be less diluted during their ascent and thus to develop higher. In the following, we will compare the vertical kinetic energy of the overshooting

parcels as predicted by one parameterization of deep convection with the values found in our giga-LES.

#### 4. Parameterization of the overshoot transport

The transport of water by convection into the stratosphere occurs inside the overshoots whose width ranges between about 10 km at the tropopause and 1 km at their top. In the atmospheric models that run at resolution coarser than 10 km, this transport can be accounted for by any deep convective parameterization. In this section, we aim at testing the capability of such a parameterization to represent the overshoot transport. The formulation of the Kain–Fritsch–Bechtold parameterization (KFB; Bechtold et al. 2001), which is that used in the Meso-NH model, is selected. It is compared to the properties of the updrafts inside the overshoots of the giga-LES. In KFB, the convective upward motions are represented by a mean subgrid updraft. The vertical velocity  $w_u$  of the subgrid updraft is assumed as

$$\frac{\Delta w_u^2}{\Delta z} = \frac{2}{1 + \gamma} B(z) - \varepsilon(z) w_u^2, \quad (1)$$

where  $\Delta z$  is the vertical resolution;  $B(z) = g(\theta_v^u - \theta_v^e)/\theta_v^e$  is the buoyancy of the subgrid updraft;  $\theta_v^u$  and  $\theta_v^e$  are the virtual potential temperature in the updraft and in the environment, respectively;  $\varepsilon(z)$  is a term proportional to the entrainment by the updraft; and  $\gamma = 0.5$  is a virtual mass coefficient that approximately takes into account nonhydrostatic pressure perturbations. The entrainment term accounts for zero environmental momentum. It is in general at least one order of magnitude lower than the buoyancy term. The variations of  $w_u^2$  are thus driven by the buoyancy to first order. For the updrafts inside the hydrating overshoots of the giga-LES,  $w_u^2$  reaches a maximum in the TTL and decreases steadily above, up to their top (Figs. 9a–c). The buoyancy  $B$  of all the overshoots is negative above 13 km, down to  $-0.2 \text{ m s}^{-2}$  at 16-km altitude. Aloft, it decreases sharply down to  $-0.8 \text{ m s}^{-2}$  in the lowermost stratosphere, where the vertical gradient of environmental potential temperature is larger than in the troposphere. The decrease of  $w_u^2$  does not show a clear relationship with the amplitude of the negative buoyancy (Fig. 9d). The scaling relation between the two parameters suggested by KFB (solid line) does not correspond to the variations observed in our giga-LES: the decrease of  $w_u^2$  as a function of  $B$  is overestimated. In principle, parameter  $\gamma$  allows us however to tune the scaling relation. Our results indicate that a larger value of  $\gamma$ , by at least one order of magnitude, better describes the slowdown of the overshoot rise in the region of negative buoyancy. The value of

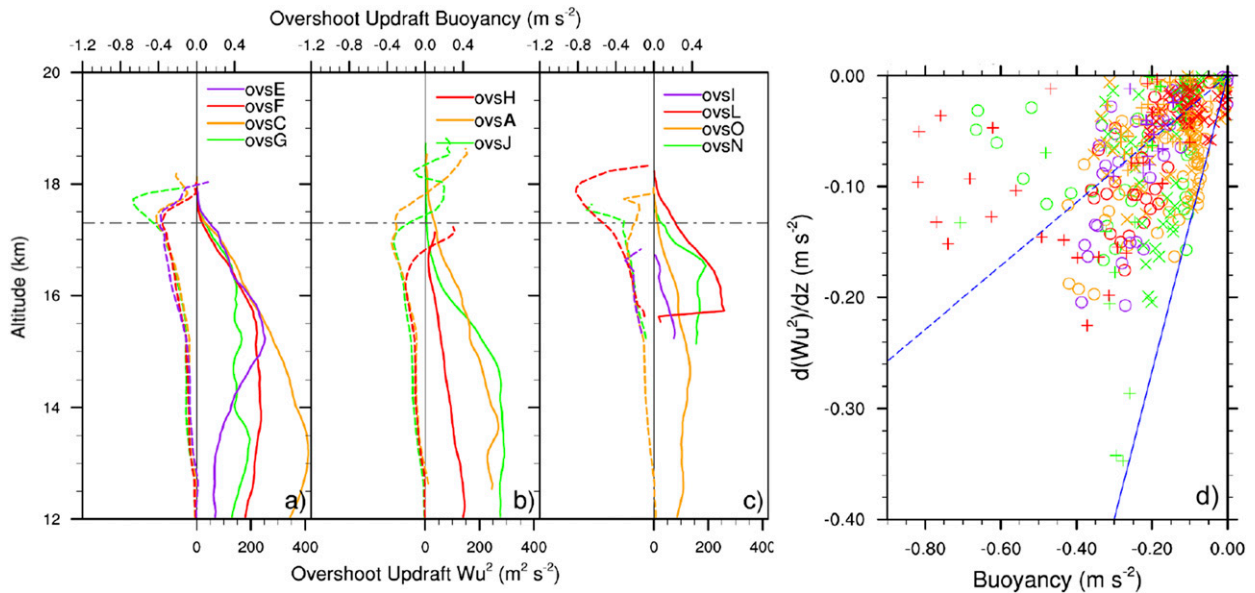


FIG. 9. Vertical profiles of the buoyancy and  $w_u^2$  for the updrafts inside the (a) most hydrating overshoots ( $+10$  to  $+100 \times 10^3$  kg of stratospheric water vapor), (b) moderately hydrating overshoots ( $+1$  to  $+10 \times 10^3$  kg), and (c) least hydrating overshoots (less than  $+1 \times 10^3$  kg). In (a)–(c), the dotted–dashed gray line is the tropopause at 380-K potential temperature. (d) Variations of  $w_u^2$  with altitude as function of the buoyancy ( $\circ$  for the most hydrating,  $\times$  for the moderately hydrating, and  $+$  for the least hydrating overshoots). The blue solid line corresponds to the KFB as it is currently implemented in Meso-NH ( $\gamma = 0.5$ ). The dashed line gives the relation obtained by linear regression:  $\gamma = 6.1$ . Only the negative values of buoyancy and  $dw_u^2/dz$  are represented and accounted for by the linear regression.

$\gamma = 0.5$  is selected on the basis of a simple theory for a spherical bubble of buoyant fluid. A larger value of  $\gamma$  would imply either that the mass of surrounding fluid moving with the overshooting air mass is significantly larger or that the spherical bubble perspective is no longer valid above the level of neutral buoyancy. Note that the entrainment term  $-\varepsilon(z)w_u^2$  in (1) can only act to make the rate of change  $\Delta w_u^2/\Delta z$  more negative; that is, the solid line in Fig. 9d corresponds to zero entrainment, and adding any entrainment will worsen the agreement between the parameterization and the values actually seen in the simulation. For this reason, the increase of  $\gamma$  seems necessary in the region of negative buoyancy.

## 5. Discussion

In the upper troposphere and higher, the concentrations of water vapor in the convective plume are sufficiently small that the dynamical role of latent heating by microphysical processes is negligible. The penetration of the convective plume from the upper troposphere into the lower stratosphere is therefore essentially a problem in classical fluid dynamics, where a negatively buoyant plume penetrates a stably stratified medium. This is an example of what is often called a “fountain” in the fluid dynamics literature, that is, a steadily supplied injection of negatively buoyant fluid. There have been several

previous studies on this problem, most using a combination of laboratory experiments and simple theory, though relatively few of these consider a case where the plume encounters a tropopause-like sharp change in stratification. In agreement with our results, the reviewed studies highlight that the maximum penetration height is a key parameter to characterize the impact of the fountain. The maximum penetration height determines the altitude of the fluid detrainment in the presence and absence of external shear (Ansong et al. 2008, 2011) and the rate of entrainment of upper-layer fluid into the fountain (Lima Neto et al. 2016). The key role of the entrainment from above was already highlighted by Cardoso and Woods (1993) and Lima Neto et al. (2016). Further studies are cited in the review by Hunt and Burridge (2015), though they highlight that the precise nature and rate of entrainment at fountain top remain unexplained. The primary questions of relevance to the overshooting convection discussed in this paper are, knowing the characteristics of the plume as it enters the region of strong stratification, 1) how far does it penetrate into that region and, 2) in particular, at what level does the intrusion spread out, or equivalently what is the density of the intrusion? The extent to which these questions are answered by existing results in the fluid dynamics literature or, if not, whether they could be addressed by straightforward extension to those results requires further consideration.

Multiple dynamical processes can cause the intense mixing between tropospheric and stratospheric air inside the overshoot (Fig. 6, left). One mechanism is the generation of gravity waves by the overshoots that then break (Lane et al. 2003). Lane et al. (2001) explain that such gravity waves are generated by the overshooting air parcels as they decelerate and oscillate around their level of neutral buoyancy (LNB) (mechanical oscillator generation). Another way to describe the wave production is the successive vortex generation with alternate directions of rotation [the vortical response to penetrative convection as demonstrated by Lane (2008)]. The gravity waves breaking can cause cross-isentropic mixing of water vapor (Wang 2003; Lane and Sharman 2006). The environmental wind shear around the tropopause is also crucial to shape the overshoots and modulates the spatial distribution of the mixing (Grabowski and Clark 1993b). For instance, the gravity waves that propagate in the same direction as the wind shear are more likely to break. The shear between the overshoot and the environment is another source of instabilities and mixing. In the frame of extratropical overshooting convection, Homeyer et al. (2017) found that the horizontal velocity difference between the cloud and the stratospheric environment is the primary factor of above-anvil cirrus formation. The horizontal wind shear, which appears very intense inside the hydrating overshoot, produce Kelvin–Helmholtz instabilities that promote mixing as they break. At even finer scales, the interface instabilities at the edge of the cloud can induce further mixing (Grabowski and Clark 1991, 1993a). However, these studies indicate that the interface instabilities only can neither fully explain the cross-isentropic transport nor the generation of a warmer, moister shell around the cold and dry overshooting core, as reported by Roach (1967). In our case, the strong wind shear appears to be the predominant process leading to intense mixing inside the overshoot.

To quantify the hydration of the stratosphere by the overshoots, microphysical processes (like vapor deposition, ice crystal growth and aggregation, ice sublimation) have to be accurately represented. In our model, a single-moment bulk microphysical scheme is used as an efficient tool that describes most important processes at a limited computational cost. Some limitations of our results are expected to derive from the use of such a scheme. In particular, the residence time of the ice hydrometeors in the lower stratosphere strongly depends on their fall speed and the efficiency of the sublimation process. On the one hand, the fall speed is determined by the size distributions of the hydrometeors, that are, in our model, governed for each bulk species by simple theoretical laws. Some secondary

processes that affect the particle sizes and concentration, like the ice breakup due to particles collisions and the explosive freezing of raindrops, as well as the limitation of the homogeneous nucleation by the lack of ice nuclei, are not taken into account, for instance. Because of these secondary processes, and independently from the concentration of ice nuclei, the ice particles are expected to be in larger number and with a smaller size than assumed by the use of our scheme. On the other hand, the rate of sublimation of the ice particles is driven by the adjustment to saturation in our model, whereas several studies reported observations of large supersaturation values inside upper-troposphere and lower-stratosphere clouds (e.g., Jensen et al. 2013). For this reason, the hydration and dehydration of the stratosphere by sublimation and deposition is expected not to be as quick as simulated here. The assessment of the overall bias is difficult to estimate since compensating errors might be at play (e.g., too-large particles but too-efficient sublimation). To overcome these limitations, further studies using a two-moment or a bin microphysical scheme are expected to shed light on the uncertainties linked with a one-moment microphysical representation.

## 6. Conclusions

The processes leading the very deep convective system Hector of 30 November 2005 to hydrate the stratosphere have been analyzed at short spatial and temporal scales. The giga-LES outputs, with a frequency of 1 min and a spatial resolution of 100 m, allow us to track and characterize the details of the 19 overshoots that penetrated the stratosphere, among the 1507 overshoots identified at the top of the deep convective system. The sequence of mechanisms that leads the overshoots to hydrate the stratosphere is (cf. Fig. 10) (i) the rise of the overshoot up to a stratospheric subsaturated layer, (ii) the entrainment of subsaturated stratospheric air into the top of the overshoot, and (iii) the mixing of the stratospheric air with the cloudy air that warms the cloud, sublimates ice particles, and forms a vapor-enriched layer at the top of the overshoot. The time scale of these mechanisms is short, on the order of 1 min, in agreement with previous numerical studies of penetrative convection (Grabowski and Clark 1991, 1993a; Lane 2008).

We highlight in this study that not all the overshoots have direct impact on the stratospheric water vapor content. The overshoots that produce no vapor-enriched air pockets are called here nonhydrating overshoots. However, the current investigation is conducted on a short time scale, and at a later time, the cloudy layers produced by the nonhydrating overshoots are continuously diluted. Ice in low concentration may either

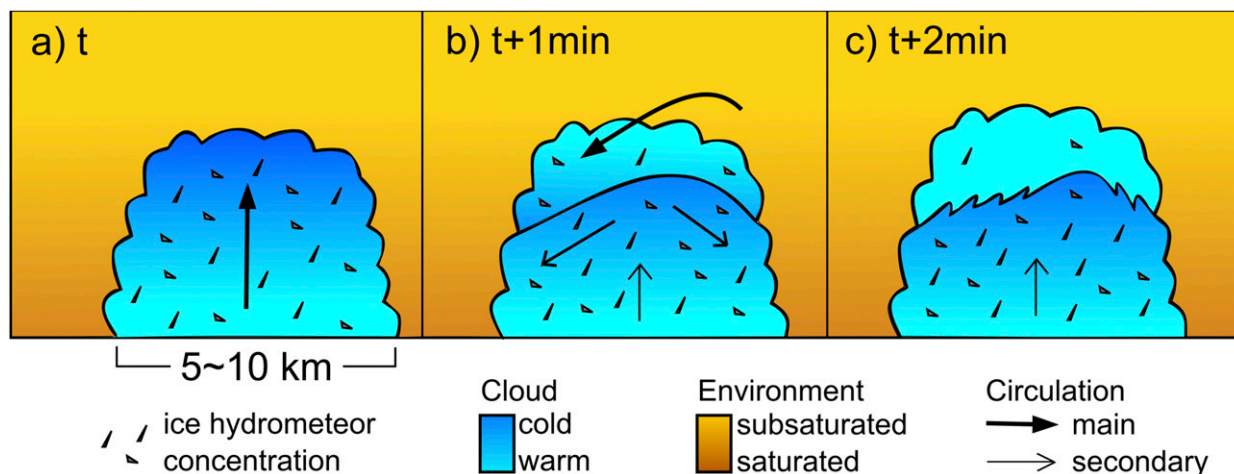


FIG. 10. Sketch of the sequence of mechanisms that leads the overshoots to hydrate the stratosphere. (a) The cold air of the overshoot rises up to the lower stratosphere. (b) Because of strongly negative buoyancy, the cold air mass collapses, entraining at its top some warmer subsaturated stratospheric air from the environment. (c) The mixing of the stratospheric air with the top of the overshoot warms the cloud, leads to the sublimation of ice particles, and forms a pocket of vapor-enriched air at the top of the overshoot. In the cloud, the blue shades indicate the temperature, with darker blue for colder regions. In the environment, the brown shades give an indication of the saturation with respect to ice, with brown for saturated regions and yellow for subsaturated regions. The arrows represent the main air motions and the triangles the ice concentration. The black line inside the cloud is the isentropic surface at 380 K that separates the cloud regions with potential temperatures typical of the troposphere (below) and stratosphere (above). In (b), the collapse of the negatively buoyant air induces strong horizontal winds. The intense wind shear generates instabilities that distort the isentropic surface at 380 K and promotes further mixing between tropospheric and stratospheric air in (c).

sediment back to the troposphere or sublimate and hydrate the stratosphere. The latter may be made possible by the slow ascent due to radiation in the TTL and the continuous mixing with the environmental air as the cloudy layer is advected and stretched by the winds.

To predict the water vapor distribution in the lower stratosphere, it is necessary to consider the combined effect of the small-scale convective injection processes described in detail in this paper and the effect of larger-scale processes. One approach is to use general circulation models and to rely on their deep convection parameterization to represent the small-scale convective transport. In the current study, the variations of the vertical velocity for the updrafts inside the overshoots have been compared to their representation by one parameterization of deep convection (KFB). Our results indicate that the damping of the vertical velocities by the negative buoyancy is too large in the present formulation of KFB. We suggest adapting the formulation in the overshoot region so that the updrafts can develop higher and reach altitudes as high as those represented in the giga-LES. Such adaptations, which better capture the effects of the overshoots above very deep convection, are expected to represent more accurately the role of overshooting convection in the transport of water and other tropospheric components (gases, aerosols) into the stratosphere in global-scale general circulation simulations.

Another approach to estimate the water vapor distribution in the lower stratosphere is to use Lagrangian trajectory models (e.g., Jensen and Pfister 2004; Fueglistaler et al. 2005; Liu et al. 2010). These models predict the water vapor based on the trajectories that air masses follow and the temperature variations that they experience, normally on the basis of large-scale meteorological fields, for example, from reanalysis or model data, which do not resolve convective injection events. Some recent trajectory calculations (e.g., Wright et al. 2011; Ueyama et al. 2018; Schoeberl et al. 2018) have attempted to take account of convection by using, for example, cloud datasets, to identify encounters of trajectories with convective systems. The estimates of the overall effect of convective injection on water vapor concentrations are variable but generally small; for example, the recent work Schoeberl et al. (2018) estimates a 1%–2% effect on the water mass in the tropical lower stratosphere. This strongly contrasts with the estimate of 18% by Dauhut et al. (2015), which was obtained by upscaling the hydration implied by the case of Hector studied here to all the convective events that penetrate above the cold-point tropopause [the number of which can be estimated from Liu and Zipser (2005)]. This estimate clearly has large uncertainty since not all very deep convective events, even if the number of such events can be estimated adequately, will produce the

same stratosphere hydration. However, the results from Lagrangian trajectory models are also uncertain since these models rely on coarse-resolution wind reanalysis fields and cloud-top altitude fields from either reanalysis or satellite observations. The present study highlights that the convective overshoots that penetrate the highest, and hence are most important for stratospheric composition (e.g., Ueyama et al. 2018), are of very small spatial and temporal scales and thus not captured by coarse-resolution reanalysis data and most likely captured inadequately by satellite observations. Furthermore, the key finding of this study is that the overshoots entrain a lot of stratospheric air across their top, a process not yet considered in Lagrangian trajectory models.

**Acknowledgments.** This research was supported by the StratoClim project funded by the European Union Seventh Framework Programme under Grant Agreement 603557 and the Idex Teasao project. Todd Lane is supported by the Australian Research Council's Centres of Excellence scheme (CE170100023). Computer resources were allocated by GENCI through Projects 90569 and 100231 (Grand Challenge Turing). Thibaut Dauhut would like to thank Patrick Mascart, who contributed to the early stage of this study via interesting discussions on the processes at play in the overshoots.

#### REFERENCES

- Adler, R. F., and R. A. Mack, 1986: Thunderstorm cloud top dynamics as inferred from satellite observations and a cloud top parcel model. *J. Atmos. Sci.*, **43**, 1945–1960, [https://doi.org/10.1175/1520-0469\(1986\)043<1945:TCTDAI>2.0.CO;2](https://doi.org/10.1175/1520-0469(1986)043<1945:TCTDAI>2.0.CO;2).
- Anderson, J. G., D. M. Wilmoth, J. B. Smith, and D. S. Sayres, 2012: UV dosage levels in summer: Increased risk of ozone loss from convectively injected water vapor. *Science*, **337**, 835–839, <https://doi.org/10.1126/science.1222978>.
- Ansong, J. K., P. J. Kyba, and B. R. Sutherland, 2008: Fountains impinging on a density interface. *J. Fluid Mech.*, **595**, 115–139, <https://doi.org/10.1017/S0022112007009093>.
- , A. Anderson-Frey, and B. R. Sutherland, 2011: Turbulent fountains in one- and two-layer crossflows. *J. Fluid Mech.*, **689**, 254–278, <https://doi.org/10.1017/jfm.2011.413>.
- Avery, M. A., S. M. Davis, K. H. Rosenlof, H. Ye, and A. E. Dessler, 2017: Large anomalies in lower stratospheric water vapour and ice during the 2015–2016 El Niño. *Nat. Geosci.*, **10**, 405–409, <https://doi.org/10.1038/ngeo2961>.
- Bechtold, P., E. Bazile, F. Guichard, P. Mascart, and E. Richard, 2001: A mass flux convection scheme for regional and global models. *Quart. J. Roy. Meteor. Soc.*, **127**, 869–886, <https://doi.org/10.1002/qj.49712757309>.
- Cardoso, S. S. S., and A. W. Woods, 1993: Mixing by a turbulent plume in a confined stratified region. *J. Fluid Mech.*, **250**, 277–305, <https://doi.org/10.1017/S0022112093001466>.
- Chaboureau, J.-P., J.-P. Cammas, J. Duron, P. J. Mascart, N. M. Sitnikov, and H.-J. Voessing, 2007: A numerical study of tropical cross-tropopause transport by convective overshoots. *Atmos. Chem. Phys.*, **7**, 1731–1740, <https://doi.org/10.5194/acp-7-1731-2007>.
- Chemel, C., M. R. Russo, J. A. Pyle, R. S. Sokhi, and C. Schiller, 2009: Quantifying the imprint of a severe Hector thunderstorm during ACTIVE/SCOUT-O3 onto the water content in the upper troposphere/lower stratosphere. *Mon. Wea. Rev.*, **137**, 2493–2514, <https://doi.org/10.1175/2008MWR2666.1>.
- Corti, T., and Coauthors, 2008: Unprecedented evidence for deep convection hydrating the tropical stratosphere. *Geophys. Res. Lett.*, **35**, L10810, <https://doi.org/10.1029/2008GL033641>.
- Dauhut, T., J.-P. Chaboureau, J. Escobar, and P. Mascart, 2015: Large-eddy simulation of Hector the Convecton making the stratosphere wetter. *Atmos. Sci. Lett.*, **16**, 135–140, <https://doi.org/10.1002/asl2.534>.
- , —, —, and —, 2016: Giga-LES of Hector the Convecton and its two tallest updrafts up to the stratosphere. *J. Atmos. Sci.*, **73**, 5041–5060, <https://doi.org/10.1175/JAS-D-16-0083.1>.
- , —, P. Mascart, and O. Pauluis, 2017: The atmospheric overturning induced by Hector the Convecton. *J. Atmos. Sci.*, **74**, 3271–3284, <https://doi.org/10.1175/JAS-D-17-0035.1>.
- de Reus, M., and Coauthors, 2009: Evidence for ice particles in the tropical stratosphere from in-situ measurements. *Atmos. Chem. Phys.*, **9**, 6775–6792, <https://doi.org/10.5194/acp-9-6775-2009>.
- Dessler, A., and Coauthors, 2016: Transport of ice into the stratosphere and the humidification of the stratosphere over the 21st century. *Geophys. Res. Lett.*, **43**, 2323–2329, <https://doi.org/10.1002/2016GL067991>.
- Frey, W., and Coauthors, 2015: The impact of overshooting deep convection on local transport and mixing in the tropical upper troposphere/lower stratosphere (UTLS). *Atmos. Chem. Phys.*, **15**, 6467–6486, <https://doi.org/10.5194/acp-15-6467-2015>.
- Fueglistaler, S., M. Bonazzola, P. H. Haynes, and T. Peter, 2005: Stratospheric water vapor predicted from the Lagrangian temperature history of air entering the stratosphere in the tropics. *J. Geophys. Res.*, **110**, D08107, <https://doi.org/10.1029/2004JD005516>.
- , A. E. Dessler, T. J. Dunkerton, I. Folkins, Q. Fu, and P. W. Mote, 2009: Tropical tropopause layer. *Rev. Geophys.*, **47**, RG1004, <https://doi.org/10.1029/2008RG000267>.
- Fujita, T. T., 1989: The Teton–Yellowstone tornado of 21 July 1987. *Mon. Wea. Rev.*, **117**, 1913–1940, [https://doi.org/10.1175/1520-0493\(1989\)117<1913:TTYTOJ>2.0.CO;2](https://doi.org/10.1175/1520-0493(1989)117<1913:TTYTOJ>2.0.CO;2).
- Grabowski, W. W., and T. L. Clark, 1991: Cloud–environment interface instability: Rising thermal calculations in two spatial dimensions. *J. Atmos. Sci.*, **48**, 527–546, [https://doi.org/10.1175/1520-0469\(1991\)048<0527:CIIRTC>2.0.CO;2](https://doi.org/10.1175/1520-0469(1991)048<0527:CIIRTC>2.0.CO;2).
- , and —, 1993a: Cloud–environment interface instability. Part II: Extension to three spatial dimensions. *J. Atmos. Sci.*, **50**, 555–573, [https://doi.org/10.1175/1520-0469\(1993\)050<0555:CEIPI>2.0.CO;2](https://doi.org/10.1175/1520-0469(1993)050<0555:CEIPI>2.0.CO;2).
- , and —, 1993b: Cloud–environment interface instability. Part III: Direct influence of environmental shear. *J. Atmos. Sci.*, **50**, 3821–3828, [https://doi.org/10.1175/1520-0469\(1993\)050<3821:CEIPI>2.0.CO;2](https://doi.org/10.1175/1520-0469(1993)050<3821:CEIPI>2.0.CO;2).
- Grosvenor, D. P., T. W. Choullarton, H. Coe, and G. Held, 2007: A study of the effect of overshooting deep convection on the water content of the TTL and lower stratosphere from cloud resolving model simulations. *Atmos. Chem. Phys.*, **7**, 4977–5002, <https://doi.org/10.5194/acp-7-4977-2007>.
- Hardiman, S. C., and Coauthors, 2015: Processes controlling tropical tropopause temperature and stratospheric water vapor in climate models. *J. Climate*, **28**, 6516–6535, <https://doi.org/10.1175/JCLI-D-15-0075.1>.



- Hassim, M. E. E., and T. P. Lane, 2010: A model study on the influence of overshooting convection on TTL water vapour. *Atmos. Chem. Phys.*, **10**, 9833–9849, <https://doi.org/10.5194/acp-10-9833-2010>.
- , —, and P. T. May, 2014: Ground-based observations of overshooting convection during the Tropical Warm Pool-International Cloud Experiment. *J. Geophys. Res. Atmos.*, **119**, 880–905, <https://doi.org/10.1002/2013JD020673>.
- Holloway, C. E., and J. D. Neelin, 2007: The convective cold top and quasi equilibrium. *J. Atmos. Sci.*, **64**, 1467–1487, <https://doi.org/10.1175/JAS3907.1>.
- Homeyer, C. R., 2015: Numerical simulations of extratropical tropopause-penetrating convection: Sensitivities to grid resolution. *J. Geophys. Res. Atmos.*, **120**, 7174–7188, <https://doi.org/10.1002/2015JD023356>.
- , J. D. McAuliffe, and K. M. Bedka, 2017: On the development of above-anvil cirrus plumes in extratropical convection. *J. Atmos. Sci.*, **74**, 1617–1633, <https://doi.org/10.1175/JAS-D-16-0269.1>.
- Hunt, G., and H. Burridge, 2015: Fountains in industry and nature. *Annu. Rev. Fluid Mech.*, **47**, 195–220, <https://doi.org/10.1146/annurev-fluid-010313-141311>.
- Jensen, E., and L. Pfister, 2004: Transport and freeze-drying in the tropical tropopause layer. *J. Geophys. Res.*, **109**, D02207, <https://doi.org/10.1029/2003JD004022>.
- , A. S. Ackerman, and J. A. Smith, 2007: Can overshooting convection dehydrate the tropical tropopause layer? *J. Geophys. Res.*, **112**, D11209, <https://doi.org/10.1029/2006JD007943>.
- , and Coauthors, 2013: Ice nucleation and dehydration in the tropical tropopause layer. *Proc. Natl. Acad. Sci. USA*, **110**, 2041–2046, <https://doi.org/10.1073/pnas.1217104110>.
- Khaykin, S., and Coauthors, 2009: Hydration of the lower stratosphere by ice crystal geysers over land convective systems. *Atmos. Chem. Phys.*, **9**, 2275–2287, <https://doi.org/10.5194/acp-9-2275-2009>.
- Kim, J., W. J. Randel, and T. Birner, 2018: Convectively driven tropopause-level cooling and its influences on stratospheric moisture. *J. Geophys. Res. Atmos.*, **123**, 590–606, <https://doi.org/10.1002/2017JD027080>.
- Lac, C., and Coauthors, 2018: Overview of the Meso-NH model version 5.4 and its applications. *Geosci. Model Dev.*, **11**, 1929–1969, <https://doi.org/10.5194/gmd-11-1929-2018>.
- Lafore, J.-P., and Coauthors, 1998: The Meso-NH atmospheric simulation system. Part I: Adiabatic formulation and control simulations. *Ann. Geophys.*, **16**, 90–109, <https://doi.org/10.1007/s00585-997-0090-6>.
- Lane, T. P., 2008: The vortical response to penetrative convection and the associated gravity-wave generation. *Atmos. Sci. Lett.*, **9**, 103–110, <https://doi.org/10.1002/asl.167>.
- , and R. D. Sharman, 2006: Gravity wave breaking, secondary wave generation, and mixing above deep convection in a three-dimensional cloud model. *Geophys. Res. Lett.*, **33**, L23813, <https://doi.org/10.1029/2006GL027988>.
- , M. J. Reeder, and T. L. Clark, 2001: Numerical modeling of gravity wave generation by deep tropical convection. *J. Atmos. Sci.*, **58**, 1249–1274, [https://doi.org/10.1175/1520-0469\(2001\)058<1249:NMOGWG>2.0.CO;2](https://doi.org/10.1175/1520-0469(2001)058<1249:NMOGWG>2.0.CO;2).
- , R. D. Sharman, T. L. Clark, and H.-M. Hsu, 2003: An investigation of turbulence generation mechanisms above deep convection. *J. Atmos. Sci.*, **60**, 1297–1321, [https://doi.org/10.1175/1520-0469\(2003\)60<1297:AIOTGM>2.0.CO;2](https://doi.org/10.1175/1520-0469(2003)60<1297:AIOTGM>2.0.CO;2).
- Lima Neto, I. E., S. S. S. Cardoso, and A. W. Woods, 2016: On mixing a density interface by a bubble plume. *J. Fluid Mech.*, **802**, R3, <https://doi.org/10.1017/jfm.2016.454>.
- Liu, C., and E. J. Zipser, 2005: Global distribution of convection penetrating the tropical tropopause. *J. Geophys. Res.*, **110**, D23104, <https://doi.org/10.1029/2005JD006063>.
- Liu, Y. S., S. Fueglistaler, and P. H. Haynes, 2010: Advection-condensation paradigm for stratospheric water vapor. *J. Geophys. Res.*, **115**, D24307, <https://doi.org/10.1029/2010JD014352>.
- Munchak, L. A., and L. L. Pan, 2014: Separation of the lapse rate and the cold point tropopauses in the tropics and the resulting impact on cloud top-tropopause relationships. *J. Geophys. Res. Atmos.*, **119**, 7963–7978, <https://doi.org/10.1002/2013JD021189>.
- Pommereau, J.-P., 2010: Troposphere-to-stratosphere transport in the tropics. *C. R. Geosci.*, **342**, 331–338, <https://doi.org/10.1016/j.crte.2009.10.015>.
- Randel, W. J., and E. J. Jensen, 2013: Physical processes in the tropical tropopause layer and their roles in a changing climate. *Nat. Geosci.*, **6**, 169–176, <https://doi.org/10.1038/ngeo1733>.
- Roach, W. T., 1967: On the nature of the summit areas of severe storms in Oklahoma. *Quart. J. Roy. Meteor. Soc.*, **93**, 318–336, <https://doi.org/10.1002/qj.49709339704>.
- Rossov, W. B., and C. Pearl, 2007: 22-year survey of tropical convection penetrating into the lower stratosphere. *Geophys. Res. Lett.*, **34**, L04803, <https://doi.org/10.1029/2006GL028635>.
- Sayres, D. S., and Coauthors, 2010: Influence of convection on the water isotopic composition of the tropical tropopause layer and tropical stratosphere. *J. Geophys. Res.*, **115**, D00J20, <https://doi.org/10.1029/2009JD013100>.
- Schoeberl, M. R., E. J. Jensen, L. Pfister, R. Ueyama, M. Avery, and A. E. Dessler, 2018: Convective hydration of the upper troposphere and lower stratosphere. *J. Geophys. Res. Atmos.*, **123**, 4583–4593, <https://doi.org/10.1029/2018JD028286>.
- Sherwood, S. C., J. Chae, P. Minnis, and M. McGill, 2004: Underestimation of deep convective cloud tops by thermal imagery. *Geophys. Res. Lett.*, **31**, L11102, <https://doi.org/10.1029/2004GL019699>.
- Smith, J. B., and Coauthors, 2017: A case study of convectively sourced water vapor observed in the overworld stratosphere over the United States. *J. Geophys. Res. Atmos.*, **122**, 9529–9554, <https://doi.org/10.1002/2017JD026831>.
- Steinwagner, J., S. Fueglistaler, G. Stiller, T. von Clarmann, M. Kiefer, P.-P. Borsboom, A. van Delden, and T. Röckmann, 2010: Tropical dehydration processes constrained by the seasonality of stratospheric deuterated water. *Nat. Geosci.*, **3**, 262–266, <https://doi.org/10.1038/ngeo822>.
- Ueyama, R., E. J. Jensen, and L. Pfister, 2018: Convective influence on the humidity and clouds in the tropical tropopause layer during boreal summer. *J. Geophys. Res. Atmos.*, **123**, 7576–7593, <https://doi.org/10.1029/2018JD028674>.
- Virts, K. S., and R. A. Houze Jr., 2015: Clouds and water vapor in the tropical tropopause transition layer over mesoscale convective systems. *J. Atmos. Sci.*, **72**, 4739–4753, <https://doi.org/10.1175/JAS-D-15-0122.1>.
- Wang, P. K., 2003: Moisture plumes above thunderstorm anvils and their contributions to cross-tropopause transport of water vapor in midlatitudes. *J. Geophys. Res.*, **108**, 4194, <https://doi.org/10.1029/2002JD002581>.
- Wright, J. S., R. Fu, S. Fueglistaler, Y. S. Liu, and Y. Zhang, 2011: The influence of summertime convection over Southeast Asia on water vapor in the tropical stratosphere. *J. Geophys. Res.*, **116**, D12302, <https://doi.org/10.1029/2010JD015416>.
- Wu, D. L., W. G. Read, A. E. Dessler, S. C. Sherwood, and J. H. Jiang, 2005: UARS/MLS cloud ice measurements: Implications for H<sub>2</sub>O transport near the tropopause. *J. Atmos. Sci.*, **62**, 518–530, <https://doi.org/10.1175/JAS-3382.1>.